Using Nanoparticle-Filled Microcapsules for Site-Specific Healing of Damaged Substrates: Creating a "Repair-and-Go" System

German V. Kolmakov,[†] Ravindra Revanur,[‡] Ravisubhash Tangirala,[‡] Todd Emrick,[‡] Thomas P. Russell,[‡] Alfred J. Crosby,[‡] and Anna C. Balazs[†,*]

[†]Chemical Engineering Department, University of Pittsburgh, Pittsburgh, Pennsylvania 15261 and [‡]Polymer Science and Engineering Department, University of Massachusetts, Amherst, Massachusetts 01003-9263

ABSTRACT Using a hybrid computational approach, we simulate the behavior of nanoparticle-filled microcapsules that are propelled by an imposed shear to move over a substrate, which encompasses a microscopic crack. When the microcapsules become localized in the crack, the nanoparticles can penetrate the capsule's shell to bind to and fill the damaged region. Initially focusing on a simple shear flow, we isolate conditions where the microcapsules become arrested in the cracks and those where the capsules enter the cracks for a finite time but are driven to leave this region by the imposed flow. We also characterize the particle deposition process for these two scenarios, showing that the deposition is greater for the arrested capsules. We then determine the effect of utilizing a pulsatile shear flow and show that this flow field can lead to an effective "repair-and-go" system where the microcarriers not only deliver a high volume fraction of particles into the crack but also leave the fissure and, thus, can potentially repair additional damage within the system.

KEYWORDS: computer simulation · microcapsules · nanoparticles · surfaces · cracks

Materials' surfaces and surface coatings are commonly exposed to severe conditions that can lead to the onset of local defects, such as surface cracks. These defects limit the performance of materials, notably affecting properties such as light transmission, reflectivity, mechanical stability, or electrical conductivity. One common strategy for repairing such damaged surfaces involves the application of a new overcoat layer with optical, mechanical, and electrical properties that match the underlying substrate and properly designed adhesive properties to establish a strong interface with the substrate. For precision fabricated materials, the application of a new overcoat layer is not optimal since the uniform finish and controlled thickness of the original parts can be sacrificed. Additionally, residual stresses can often develop during curing that limit the lifetime of the repaired part. Therefore, the ability to selectively repair a surface defect or crack is especially attractive.

Previously, Balazs *et al.* modeled the rolling motion of a fluid-driven, particle-filled microcapsule along a heterogeneous, adhesive substrate to determine how the release of the encapsulated nanoparticles could be harnessed to repair damage on the underlying surface.[1] The simulations revealed that these microcapsules can deliver the encased materials to specific sites on the substrate, effectively generating an alternate route to repairing surface defects. Once the healing nanoparticles were deposited on the desired sites, the fluid-driven capsules could move further along the surface, and for this reason, the strategy was termed "repair-and-go". The latter strategy could be particularly advantageous since it would have negligible impact on the precision of the nondefective regions and involves minimal amounts of the repair materials.

Herein, we extend the prior two-dimensional model[1] to simulate the three-dimensional interactions of deformable microcapsules with a substrate that contains a 3D crack. While the parameter space we consider is relatively general, we nonetheless were inspired by particular, experimentally realizable systems.[2−7] Specifically, we assumed that the surfaces of the microcapsules are amphiphilic in nature and, thus, could have comparable interactions with hydrophilic and hydrophobic domains. Such microcapsules can be fabricated from comb copolymers that encompass a hydrophobic backbone and hydrophilic side chains.[2] We further assume that the

*Address correspondence to balazs@pitt.edu.

Received for review September 25, 2009 and accepted January 12, 2010.

Published online January 20, 2010.
10.1021/nn901296y

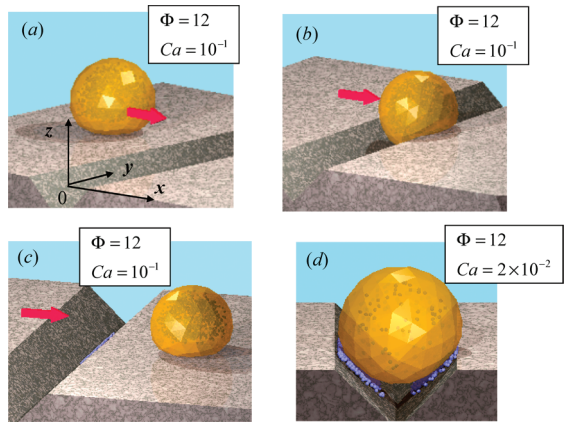

Figure 1. Graphical output from the simulation showing the motion of a capsule on a damaged surface from its initial position (a) to the interior of the crack (b) and its re-emergence onto the undamaged portion of the surface (c). For this case, the capillary number Ca = 10^{-1} and dimensionless adhesion strength Φ = 12. The gray shaded areas mark the substrate, and the blue points correspond to the nanoparticles. Red arrows indicate the direction of the imposed shear flow. (d) Capsule arrested within the crack at Ca = 2 × 10^{-2} and Φ = 12.

microcapsules encase an oil phase, which contains dispersed hydrophobic nanoparticles. Again, this aspect of the model can be experimentally realized. In particular, the encapsulated particles could be quantum dots that were functionalized with hydrophobic ligands.[3,4] Within an oil/water mixture, the amphiphilic comb copolymers can out-compete the functionalized quantum dots for an oil-in-water droplet interface and, thus, provide an encapsulating shell for the coated nanoparticles, which are dispersed in the interior oil phase.[3,4] Upon cross-linking of the polymer shell, the copolymers form a robust microcarrier for the nanoparticles, with a very thin (~10 nm) wall[3,4] through which the nanoparticles can permeate under appropriate conditions.

In the simulation, we assume that the hydrophilic surface contains a crack, and the interior of this crack is assumed to be hydrophobic. This substrate can be fabricated from poly(dimethyl siloxane) (PDMS)-based polymers with brittle surfaces. PDMS is hydrophobic, but ultraviolet/ozone (UVO) treatment effectively converts the surface of a PDMS film from hydrophobic to hydrophilic, by production of a thin silica-like surface layer (having a very low water contact angle).[8] The surface silica layer has a higher modulus than the underlying PDMS.[9] Subjecting such PDMS−silica composite films to strain forces (either mechanical or osmotic) that exceed the failure strain of the surface coating leads to cracking at the surface. Osmotic strain (generated by swelling the underlying PDMS in hexanes) results in formation of random cracks on the PDMS surface; mechanical stain (uniaxial extension) generates the aligned cracks.[10]

With the above materials in mind, we simulate the scenario shown in Figure 1, where hydrophobic nanoparticles are encapsulated in a fluid-filled microcapsule, which is localized on a substrate in an aqueous solution. The intact portion of the surface is hydrophilic, but this substrate also encompasses cracks, which expose the underlying hydrophobic domains (*e.g.*, the underlying PDMS). The amphiphilic nature of the capsule allows this colloid to be solubilized in water and attracted to both hydrophilic and hydrophobic portions of the surface. On the other hand, the encapsulated hydrophobic nanoparticles are only attracted to the hydrophobic cracks.

In effect, the enthalpic interactions between the nanoparticles and the hydrophobic crack provide a site-specific response of these particles. As we show below, when the capsule is localized in the crack, the nanoparticles can tunnel through the microcapsule's shell to bind to and fill the cracked regions. Below, we also determine the conditions for optimizing the performance of this repair process. In particular, we find that the application of a nonsteady, pulsatile flow field could be useful in maximizing the deposition of particles into the crack and sustaining the continued motion of microcapsules, therefore crucially increasing the effectiveness of the autonomous healing of a damaged surface.

It is noteworthy that micrometer-sized capsules filled with dissolved particles can encompass very high payloads, allowing them to rapidly carry and deliver large amounts of nanoparticles to a desired location. Furthermore, the continued, flow-driven motion of these microcarriers potentially allows multiple damaged regions to be healed by the capsules.

To simulate this multicomponent system, which involves complex fluid−structure interactions between the solution and the capsule, as well as the diffusion of nanoparticles, we take advantage of our recently developed hybrid "LBM/LSM" technique.[11−16] In this approach, the dynamic behavior of the encapsulated and external host fluids is captured through the lattice Boltzmann model (LBM) for hydrodynamics. The capsule's shell and the underlying surface are modeled through the lattice spring model (LSM) for the micromechanics of elastic solids. In this integrated LBM/LSM method, the fluid and solid components interact through appropriate boundary conditions at the solid−fluid interface. We augment this LBM/LSM approach by introducing a Brownian dynamics simulation[1,17,18] to model the diffusion of the nanoparticles within the system.

We note that these microcapsules effectively mimic some of the functionality of biological leukocytes in that they localize at damaged sites and facilitate the repair process. As the introduction of a synthetic microvasculature[19] into structural materials becomes more developed, the use of such microcapsules as cellular mimics could expand the efficiency of the artificial circulatory systems. In addition to supplying healing reagents in the channels, it could be advantageous to en-

capsulate "damage markers" within the microcapsules. The microcapsules could continue to circulate in a "healthy", undamaged system but become trapped or localized at a damaged site and thereby deliver a chemical "marker" (*i.e.*, a visible or fluorescent dye) through its porous shell. Such markers will enable one to nondestructively locate and track the damaged regions over time.

RESULTS AND DISCUSSION

Effect of Imposing a Steady Shear Flow. Using the model described in the Methodology section, we determine conditions that provide maximal deposition of nanoparticles into the surface crack and, thereby, produce effective repair of the substrate. We focus on a single capsule that interacts with a bare crack to gain insight into the initial steps involved in coating the surface and to establish optimal conditions early in the deposition process. Additional fluid-driven capsules moving along the surface are needed to continue the selective delivery of the fillers into the damaged regions. Below we also examine the interactions between a microcarrier and a partially filled fissure and then, finally, investigate the behavior of a microcapsule on a surface containing a nanoparticle-filled, "healed" domain.

The simulation box is $L_x \times L_y \times L_y = 100 \times 40 \times 40$ lattice Boltzmann units in size. Periodic boundary conditions are applied in the *x*- and *y*-directions. A well-defined crack is located in the center of the substrate along the *y*-axes, with the crack tip being located at $x = 0$ (see Figure 1). The capsule diameter is equal to $10\Delta x$, where Δx is equal to the lattice spacing in the LBM. The crack depth, d_c, is equal to $5\Delta x$ (*i.e.*, comparable to the capsule radius), and the crack width is equal to $2d_c$.

The flat, upper wall of the simulation box is moved with a constant velocity U_{wall} to create a uniform shear rate of $\dot{\gamma} = U_{wall}/L_z$. We characterize the flow by specifying the dimensionless capillary number $Ca = \dot{\gamma}\mu R/Eh$, where μ is the fluid viscosity, R is the capsule radius, E is the modulus of the shell, and h is the shell thickness.[12,13] The capillary number represents the relative importance of the viscous stress in the surrounding fluid and the elastic stress in the capsule's shell. In the simulations, we vary Ca by altering $\dot{\gamma}$, keeping the values of the other relevant parameters fixed. In the ensuing studies, we consider capillary numbers in the range of $10^{-4} \leq Ca \leq 10^{-1}$, which are experimentally reasonable values if we consider the microcapsules to be propelled by an imposed flow in an aqueous solution whose viscosity is $\mu \approx 10^{-3}$ kg/sm and density is $\rho \approx 10^3$ kg/m^3. Typical velocities in microfluidic devices are on the order of 1 cm/s, and typical channel heights are hundreds of micrometers.[20] For polymeric microcapsules with a diameter of 10 μm, the stiffness of the shell, Eh, can be on the order of $10^{-3}-1$ N/m.[21,22] From these values, we obtain capillary numbers of $Ca \sim 10^{-5}-10^{-2}$, which is approximately the range considered in these simulations.

We also introduce a dimensionless interaction strength[12,13] $\Phi = \varepsilon N/Eh\kappa^2$, where ε and κ characterize the respective strength and range of the interaction potential; here, N is the number of nodes on the capsule's outer surface. The parameter represents Φ, the ratio of the interaction strength to the membrane stiffness. For $\Phi \gg 1$, this interaction leads to significant deformation of the capsule, while for $\Phi \ll 1$, the effect on the capsule's shape is small. Herein, we consider $0 < \Phi < 25$, which also corresponds to experimentally realistic values.[13] (By expressing the data in terms of such dimensionless numbers, we can provide more flexible guidelines for potential experimental studies. In the case of the capillary number and interaction strength, the experimentalist is free to choose, for instance, a combination of capsule sizes, Young's modulus, and shell thickness that will result in the specified ratio.)

We focus primarily on the case where the interaction of the microcapsule with the undamaged horizontal substrate and with the crack walls is characterized by the same interaction constant ε. As noted in the previous section, the surface of the microcapsule is assumed to be amphiphilic, and thus, it can exhibit a comparable interaction with both the intact hydrophilic surface and the hydrophobic crack. We also investigate one case where the capsule is less attracted to the hydrophobic than the hydrophilic region; we simulate this case by setting the interaction strength within the crack to half the value for the rest of the substrate. In all of the simulations, we further assume that the deposited hydrophobic nanoparticles do not modify the adhesive properties of the crack walls. (The latter choice is not a necessary constraint of the method: the nanoparticles can dynamically modify the adhesive properties in the simulation.[1])

As shown in Figure 1a, the capsule is initially placed on the undamaged, horizontal region of the surface (with its center of mass positioned at $x = -15$) and in the middle of the channel in the *y*-direction (at $y = 20$). The capsule initially contains $N_{NP}(0) = 10^5$ nanoparticles. The particle-filled capsule is propelled toward the crack by the imposed shear flow; the red arrow in Figure 1a shows the direction of the imposed shear. The images in Figure 1b,c are for a capillary number of $Ca = 10^{-1}$ and adhesion strength of $\Phi = 12$ and correspond to points in time when the capsule is localized in the crack (Figure 1b) and when it has been propelled away from this region by the imposed flow (Figure 1c). For the image in Figure 1d, the adhesion strength is held fixed, but the shear rate is decreased to $Ca = 2 \times 10^{-2}$ and the figure shows that capsule has become arrested in the crack as it moved along the surface.

Figure 2 shows the time dependence of the capsule's center-of-mass *x*-coordinate for $\Phi = 2.4$ and for

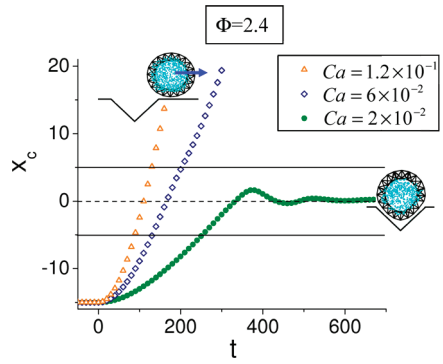

Figure 2. Center-of-mass coordinate x_c of a capsule as a function of time. The respective shear rates are labeled on the plot. Open symbols are for moving capsules, and the filled symbols are for the arrested capsule. The *x*-coordinates of the crack boundaries are indicated by the solid horizontal lines, and the *x*-coordinate of the crack tip is shown by a dashed horizontal line. Damped oscillations of an arrested capsule (green circles) in a crack (see Figure 1d) are clearly seen at $t > 350$.

three shear rates, corresponding to Ca $= 2 \times 10^{-2}$, 6×10^{-2}, and 1.2×10^{-1}. Additionally, in Figure 3, we plot a phase map for the system as a function of Ca and Φ that indicates the response of the capsules to the imposed flow and the attractive surface. To generate this phase map, we varied the dimensionless interaction strength from weak to strong adhesion, $3 \times 10^{-2} \leq \Phi \leq 24$, and the shear rates, Ca, from 2.7×10^{-4} to 1.2×10^{-1}. For each point, we averaged over three independent runs. In Figure 3a, the interaction strengths of the amphiphilic microcapsule with the undamaged

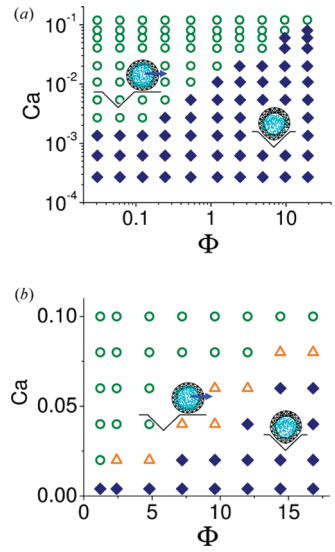

Figure 3. (a) Numerically calculated phase map as a function of capillary number Ca and interaction strength Φ. The unfilled circles indicate moving capsules, and the solid diamonds indicate arrested capsules. The interaction strengths characterizing the intact surface and within the crack are the same. (b) Phase map computed for the case where the interaction strength within the crack is equal to half the interaction strength Φ for the rest of the substrate. Open triangles shows the points on the map at which the microcapsule changes its behavior from an arrested state (at plot a) to a moving state when the interaction within the crack is reduced.

(ε_u) and damaged (ε_d) regions of the substrate are equal. These results reveal two general scenarios for the capsule's motion. For relatively high adhesion or low shear rates (indicated by the solid diamonds in the phase map), the capsule becomes arrested within the crack (as shown in Figure 1d). For weaker adhesion and higher shear rates (marked by the empty circles), the capsule moves into the crack but then exits this region to continue moving along the surface (as seen in Figure 1c). In rare events, after the capsule leaves the crack, it bounds off the substrate due to lift forces that arise at high shear rates.

In Figure 3b, the interaction parameters between the capsule and the damaged and undamaged regions have different values; here, $\varepsilon_d = 1/2\varepsilon_u$. (The latter values were chosen to illustrate the effect of having $\varepsilon_d \neq \varepsilon_u$.) In other words, Φ for the capsule and the crack is one-half of that for the capsule and undamaged substrate. For the unfilled triangles on the phase map, the capsule is arrested in the crack for $\varepsilon_d = \varepsilon_u$ but becomes free when $\varepsilon_d = 1/2\varepsilon_u$. (To make these differences more visible, we plot the map on Figure 3b in a linear scale.) It is clear from the plot that the microcapsule leaves the less adhesive crack at smaller shear rates. Nonetheless, the overall character of the phase map for the two cases remains unchanged.

To characterize the nanoparticle layer deposited by the microcapsule onto the crack walls and, hence, quantify the extent of the repair, we calculated $N_{dep}(t)$, the total number of nanoparticles deposited by time *t*. Figure 4 shows the behavior of $N_{dep}(t)$ as a function of time for an arrested (Figure 4a) and a moving (Figure 4b) capsule; here, the quantity is normalized to the total number of nanoparticles initially encased in the microcapsule, $N_{NP}(0)$. For an arrested capsule, the ratio $N_{dep}(t)/N_{NP}(0)$ approaches unity. The total number of deposited nanoparticles provided by a moving capsule, however, is smaller. For example, we obtain $N_{dep}(t)/N_{NP}(0) \sim 0.08$ for the case shown in Figure 4b.

To further characterize the performance of the microcarriers, we calculate $N_{NP}(t) = N_{NP}(0) - N_{dep}(t)$, the number of nanoparticles that remain within the capsule as a function of time. In Figure 5a, we plot, $N_{NP}(t)$ on a semilogarithmic scale for two different points (Φ,Ca) within the "arrested" region of the phase map in Figure 3. The parameter t_{in} indicates the time when the capsule becomes arrested in the crack, and hence, the nanoparticles begin to be deposited in this region. Figure 5a indicates that, at $t > t_{in}$, the temporal dependence of $N_{NP}(t)$ can be approximated by an exponentially decaying function of the form

$$N_{NP}(t) = N_{NP}(0)\exp[-(t - t_{in})/\tau_{dep}] \qquad (1)$$

with a characteristic deposition time τ_{dep}. According to eq 1, approximately $(1 - e^{-1}) \times 100\% \approx 63\%$ of the nanoparticles initially placed in the capsule are depos-

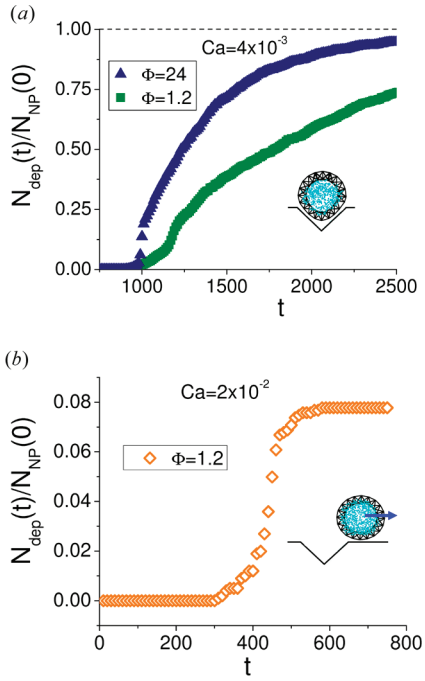

Figure 4. Time dependence of $N_{dep}(t)$, the number of nanoparticles deposited on the crack surface. The number is normalized to the initial number of nanoparticles in the capsule $N_{NP}(0)$. (a) Solid symbols indicate arrested capsules. (b) Unfilled symbols indicate moving capsules. Respective values of Ca and Φ are marked on the plot.

ited into the crack during the time period τ_{dep} after the capsule was arrested. An amount $(1 - e^{-2}) \times 100\% \approx$ 86% of nanoparticles are deposited after the time period $2\tau_{dep}$ and greater than 95% of nanoparticles are deposited after the time period $>3\tau_{dep}$.

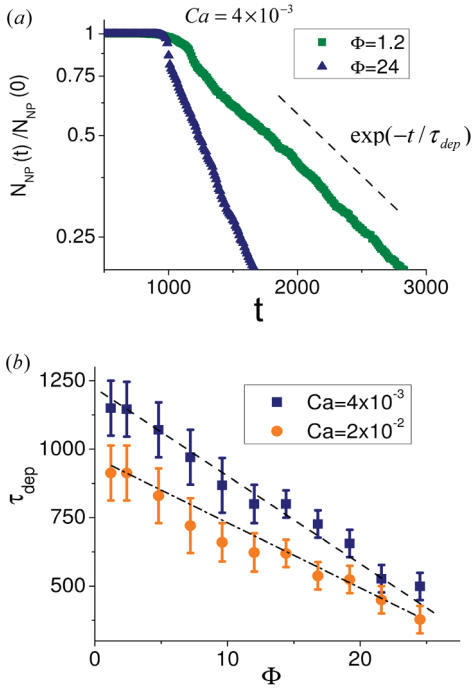

Figure 5. (a) Number of nanoparticles within an arrested capsule normalized to its initial value, $N_{NP}(t)/N_{NP}(0)$, plotted as a function of time on a semilogarithmic scale. The capillary number is Ca = 4 × 10^{-3}. Dashed line shows an exponential dependence $N_{NP}(t) \sim \exp(-t/\tau_{dep})$ with a characteristic deposition time τ_{dep}. (b) Dependence of the deposition time τ_{dep} on the dimensionless interaction strength Φ plotted for Ca = 4 × 10^{-3} and 2 × 10^{-2}. Straight lines are plotted as a guide for the eye.

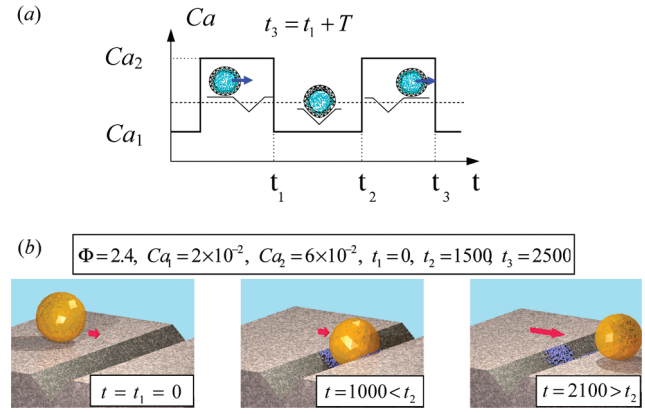

Figure 6. (a) Schematic indicating the time dependence of Ca (and thus, $\dot{\gamma}$) for the imposed pulsatile shear flow. The t_1, t_2, and t_3 are the points in time when the shear rate is switched. A horizontal dashed line shows the ordinate of the boundary between the regions in Figure 3a where the capsule is free (unfilled circles) and arrested (filled diamonds) for a given value of interaction strength Φ. The capillary number Ca_1 belongs to an arrested state, and the capillary number Ca_2 belongs to a moving state of the capsule. (b) Motion of the capsule computed for $t_1 = 0$, $t_2 = 1500$, $t_3 = 2500$, Φ = 2.4, $Ca_1 = 2 \times 10^{-2}$, and $Ca_2 = 6 \times 10^{-2}$. Left frame: initial position of the capsule. Middle: capsule arrested within the crack during the low-shear period, $t_1 < t < t_2$. Right: capsule leaves the crack at $t > t_2$. The length of the red arrow is proportional to the applied shear rate.

Figure 5b shows the dependence of the deposition time τ_{dep} on the interaction strength Φ at two shear rates for capsules that are arrested in the crack. The results are averaged over three independent runs. The deposition time τ_{dep} is seen to decrease with an increase in the interaction strength. The reason for this behavior can be explained as follows. At moderate adhesion ($\Phi \sim 1$), a spherical capsule arrested within the crack is essentially undeformed and, therefore, has only a small contact area with the crack walls. At higher adhesion ($\Phi \gg 1$), the capsule is deformed by the attractive interaction with the substrate and, thus, the contact area and the average distance r between the shell and the walls is decreased. Since the probability for nanoparticles to be deposited onto the crack wall rises rapidly with decreasing r (see eq 5), the deposition time τ_{dep} is a decreasing function of the interaction strength. In other words, a shorter time is required for achieving higher coverage for strong adhesion strengths.

Figure 5b also indicates that the deposition time is shorter for relatively larger shear rates. For Ca ≥ 2 × 10^{-2}, the fluid acts to deform the capsule[12−16] and, thus, again produces an increase in the contact area between the capsule and surface and a decrease in the distance r.

We now turn our attention to the case of a nonarrested or "free" capsule, which leaves the crack and continues to move along the surface under the imposed flow (the parameters are marked by the circles in Figure 3). For these cases, the number of deposited nano-

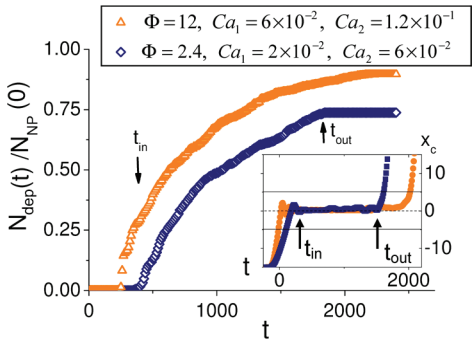

Figure 7. Time dependence of the nanoparticle coverage calculated for the pulsatile shear shown for two different values of the interaction strength. Inset shows the time dependence of the center-of-mass *x*-coordinate of the capsule calculated for the same parameter set as in the main plot. The colors of symbols in the inset match the colors in the main plot. Arrows mark the moments of time when the capsule was arrested in (t_{in}) and exits the crack (t_{out}) for $\Phi = 2.4$ (blue symbols). In the simulations, we take $t_1 = 0$, $t_2 = 1500$, $t_3 = 2500$.

particles, N_{dep}, is relatively small (see Figure 4) as compared to the number obtained with an arrested capsule. The reasons for the observed decrease in the effectiveness of these moving capsules are two-fold. First, the average distance r between the capsule shell and the crack walls is large in comparison with the characteristic distance κ for nanoparticle deposition. In particular, $r/\kappa \sim d_c/\kappa \sim 5$ for a capsule moving over the crack. Second, the time during which the capsule moves over the crack (≤50 simulation time steps according to Figure 2) and the nanoparticles can be deposited into this region is short compared with the deposition time $\tau_{dep} \geq 300$. As a result, it is more difficult to obtain full coverage in the case of a free capsule.

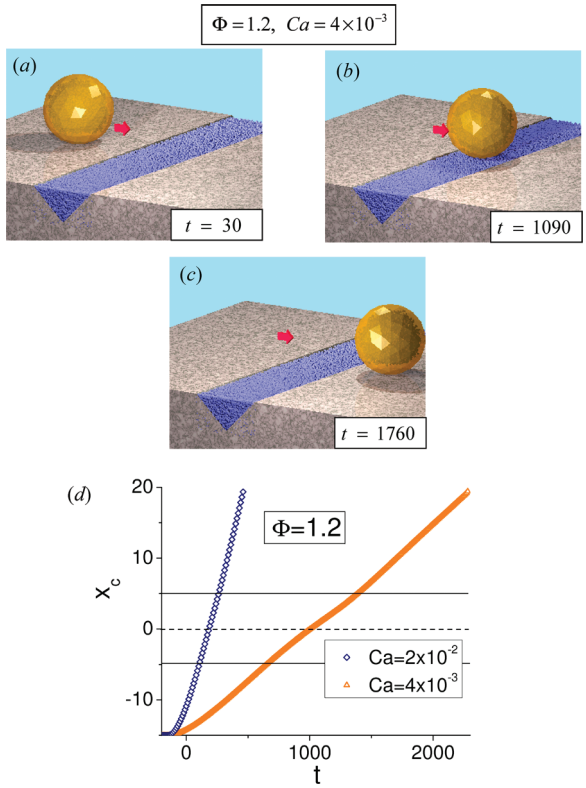

Figure 8. (a−c) Motion of the microcapsule along the surface with a crack completely filled with nanoparticles. (d) Time dependence of the center-of-mass coordinate x_c of a capsule computed for $\Phi = 1.2$ and $Ca = 2 \times 10^{-2}$ and 4×10^{-3}.

To summarize, we find that full surface coverage by the nanoparticles can be more readily attained in the case of an arrested capsule, that is, in a "repair" rather than a "repair-and-go" system. In the next section, however, we demonstrate that a pulsatile fluid flow can lead to an effective repair-and-go scenario where the microcarriers not only deliver a high volume fraction of particles into the crack but also leave the crack and, thus, could potentially contribute to repairing additional cracks within the system with the remaining encapsulated particles.

Utility of Applying a Pulsatile Flow. In the following simulations, we apply a pulsatile shear where the value of the shear rate $\dot{\gamma}(t)$ (and, hence, the capillary number $Ca(t)$) depends on time in the manner shown in Figure 6a. In effect, we use the information from the previous section to tailor the motility of the capsule. Specifically, for a fixed Φ, we choose a low capillary number Ca_1 from the region in the phase map where the capsule is arrested within the crack. After a time interval Δt, we then increase the shear rate to Ca_2 so that, for the specific Φ, the capsule is in the free region of phase space. (We note that the capsule can move along the undamaged portion of the surface for both Ca_1 and Ca_2.) In the time interval $t_1 < t < t_2$ during which the low shear corresponding to $Ca = Ca_1$ is applied, the capsule can become arrested in a nearby crack, and if this time interval is sufficiently long, the microcarrier can deposit a high density of nanoparticles along the walls of the crack (see below). At $t = t_2$, we increase the shear rate to $Ca = Ca_2$; in other words, we move vertically up in the (Φ,Ca) phase map. The simulations show that, at some time $t = t_{out} > t_2$, the capsule leaves the crack due to the strong drag force from the surrounding fluid and moves further along the surface.

Figure 6b shows this behavior for two parameter sets, $Ca_1 = 2 \times 10^{-2}$, $Ca_2 = 6 \times 10^{-2}$ for an adhesion strength of $\Phi = 2.4$ (the case of moderate adhesion), and $Ca_1 = 6 \times 10^{-2}$, $Ca_2 = 1.2 \times 10^{-1}$ for an adhesion strength of $\Phi = 12$ (strong adhesion). The inset in Figure 7 shows the variations with time of the center-of-mass *x*-coordinate of the capsule calculated for the two parameter sets. The capsule is arrested within the crack at a time $t = t_{in} \sim 100$ and leaves the crack at $t = t_{out} \sim 1500-2000$ in both cases. The main plot in Figure 7 shows the time dependence of the coverage computed for the two parameter sets. As can be seen, a nearly full deposition $N_{dep}/N_{NP}(0)$ (73% for moderate adhesion and 90% for strong adhesion) is obtained for a pulsatile flow. The latter values are significantly above the typical values of $N_{dep}/N_{NP}(0)$ (~10−20%) obtained

for a permanently moving or free capsule in a steady flow.

As indicated in Figure 7, the advantage of using the pulsatile shear is that we can combine high adhesion strength Φ, which provides nearly full nanoparticle coverage of the crack, with the possibility for a capsule to remain moving along the surface, therefore realizing the basic ideas of a repair-and-go system. Additionally, by applying a pulsatile flow, we can control the effective exposure time $t_{exp} = t_{out} - t_{in} \approx t_2 - t_1$ (see Figure 6a); that is, the exposure time can be set manually and independently and can be varied over wide limits. (In the repair-and-go system with a pulsatile shear, the exposure time t_{exp} is defined by the duration of the low shear portion $t_2 - t_1$.) Furthermore, we can exploit the attractive features offered by the case of relatively high adhesion strength; namely, the higher Φ affords a more deformable capsule, which in turn contributes to an increased healing rate (see Figure 5b).

Microcapsule Motion on a Nanoparticle-Filled Domain. In the later stages of healing, the crack is essentially filled with nanoparticles. Figure 8a−c demonstrates the motion of a microcapsule on a surface where the crack is completely filled with nanoparticles. Here, we set $\Phi = 1.2$ and $Ca = 4 \times 10^{-3}$; for these parameters, the microcapsule is arrested within the empty crack (Figure 3). It is seen, however, that, in the case of a filled crack, the microcapsule passes over the crack without being arrested. Figure 8d shows the capsule's center-of-mass coordinate as a function of time for the adhesion strength $\Phi = 1.2$ and for capillary numbers $Ca = 4 \times 10^{-3}$ and $Ca = 2 \times 10^{-2}$ (*i.e.*, for points that lie within the different regions of the phase map in Figure 3) calculated for a completely filled crack. It is clearly seen that in both cases the microcapsule moves freely along the surface under the action of an imposed shear flow.

CONCLUSIONS

The above studies were inspired by the functionality of leukocytes that respond to damage within the body by localizing at the affected areas and initiating the repair process. Leukocytes encase a host of biological machinery that enables these cells to sense the location of the wound and, subsequently, promote the cascade of dynamic events that lead to wound healing. Our aim, in essence, was to design an artificial leukocyte that could affect the repair of a synthetic wound, namely, a crack in a surface. A significant challenge is designing a system that can accomplish this goal without considerable human intervention or any of the biological machinery inherent to the cells. We are then constrained or guided by the type of experimental systems that could be synthesized for these purposes. The ability to fabricate amphiphilic capsules that encapsulate hydrophobic nanoparticles and surfaces that encase hydrophobic cracks allowed us to formulate a delivery system that could be transported by an imposed flow in an aqueous solution and specifically target the nanoparticles to the hydrophobic domains.

With the above experimental systems providing the conceptual inspiration for our studies, we used a hybrid computational model to simulate the fluid-driven motion of a compliant microcapsule on a cracked surface. These capsules encase nanoparticles, which act as the healing agents by essentially filling the fissures and, thereby, re-establishing the continuity or structural integrity of the substrate. We found that there is a range of capsule−surface interaction parameters and shear rates that maximize the deposition of the nanoparticles into the cracks. For this range of parameters, however, the capsule becomes arrested in the crack.

Our ultimate goal is to design a system where the nanoparticle-filled capsule would not only aid in the repair of one site but also travel on to heal other cracks. To this end, we introduced a pulsatile shear flow that involves alternating low and high shear rates. In the low shear rate phase, the pulsatile flow enables the capsule to be localized within a crack for a time Δt. With an increase in the shear rate, however, this capsule is propelled to leave the fissure and, thus, be available to carry out further healing of the damaged substrate. Hence, by utilizing the pulsatile flow field, we could achieve the desired repair-and-go functionality in our simulations. (An attractive feature of this system is that the user can tailor the flow profile in order to control the value of Δt.)

We note that, in the above studies, we focused on the action of a single microcapsule, allowing us to isolate the factors that control the dynamic behavior of this microcarrier. In the actual physical system, which involves a solution of microcapsules moving in a microchannel, there is a high volume fraction of microcarriers available to repair the surface, and thus, the cracks could potentially be completely filled by deposited nanoparticles. As we showed in the final section of this paper, for the chosen interaction parameters, the amphiphilic capsules would then move over these repaired areas and go onto other locations where they are needed.

METHODOLOGY

To capture the fluid−structure interactions between the flowing fluid and the surface of the compliant capsule, we used our recently developed hybrid approach,[1,11−16] which integrates the lattice Boltzmann model (LBM) for the fluid dynamics and the lattice spring model (LSM) for the micromechanics of an elastic solid. Herein, we use this approach to simulate a three-dimensional capsule that is driven by an imposed flow to move on a rigid substrate, which contains a well-defined crack. The capsule contains a solution of dispersed nanoparticles.

The capsule's elastic, solid shell is represented by a lattice spring model, which consists of a triangular network of harmonic springs that connect regularly spaced mass points, or nodes.[14−16] The spring force $\boldsymbol{F}_s$ on node $\boldsymbol{r}_i$ is equal to

$$\boldsymbol{F}_s(\boldsymbol{r}_i) = -\sum_j k_j[(r_{ij} - r_{ij}^{eq})/r_{ij}]\boldsymbol{r}_{ij} \quad (2)$$

where the summation runs over all nearest- and next-nearest-neighbor nodes. The quantity $\boldsymbol{r}_{ij} = \boldsymbol{r}_i - \boldsymbol{r}_j$ is the radius vector between ith and jth nodes, r_{ij}^{eq} is the equilibrium length of the spring, and k_j is the spring constant. To capture the dynamics of the solid shell, we numerically integrate Newton's equations of motion, $M(d^2\boldsymbol{r}_i/dt^2) = \boldsymbol{F}(\boldsymbol{r}_i)$, where M is the mass of a node. The total force $\boldsymbol{F}$ acting on a node consists of the following: the sum of the spring forces between the masses (representing the elastic response of the solid shell), the force exerted by the fluid on the shell at the fluid−solid boundary, and the adhesion forces at the solid substrate (see below).

The capsule's spherical shell is formed from two concentric layers of LSM nodes; each layer contains $N = 122$ nodes. These two layers are separated by a distance of $\Delta x_{LSM} = 1.5\Delta x$, where Δx_{LSM} is the lattice spacing between nearest nodes in the LSM and Δx is the spacing in the LBM (see below). The outer radius of the shell was taken to be $R = 5\Delta x$. For small deformations, the LSM system obeys linear elasticity theory and results in a Young's modulus of $E = 5k_j/2\Delta x_{LSM}$.[24,25]

The LBM can be viewed as an efficient solver for the Navier−Stokes equation.[23] More specifically, this lattice-based model consists of two processes: the propagation of fluid "particles" to neighboring lattice sites, and the subsequent collisions between particles when they reach a site. Here, the fluid particles are representative of mesoscopic portions of the fluid and are described by a particle distribution function $f_i(\boldsymbol{r},t)$, which characterizes the mass density of fluid particles at a lattice node $\boldsymbol{r}$ and time t propagating in the direction i with a constant velocity $\boldsymbol{c}_i$. (The velocities $\boldsymbol{c}_i$ in ith direction are chosen so that fluid particles propagate from one lattice site to the next in exactly one time step Δt.) The time evolution of these distribution functions is governed by a discretized Boltzmann equation.[23] In three-dimensional systems, the simulations involve a set of 19 particle velocity distribution functions at each node. The hydrodynamic quantities of interest are moments of the distribution function, that is, the mass density $\rho = \sum_i f_i$, the momentum density $\boldsymbol{j} = \rho\boldsymbol{u} = \sum_i \boldsymbol{c}_i f_i$, with $\boldsymbol{u}$ being the local fluid velocity, and the momentum flux $\Pi = \sum_i \boldsymbol{c}_i\boldsymbol{c}_i f_i$.

In our LBM/LSM simulations, the fluid and solid phases interact through appropriate boundary conditions.[11−13] In particular, lattice spring nodes that are situated at the solid−fluid interface impose their velocities on the surrounding fluids; the velocities are transmitted through a linked bounce-back rule[26] to those LBM distribution functions that intersect the moving solid boundary. In turn, LS nodes at the solid−fluid interface experience forces due to the fluid pressure and viscous stresses at that boundary. We calculate the latter force based on the momentum exchange between the LBM particle and solid boundary and then distribute this quantity as a load to the neighboring LS nodes. We further assume no-slip boundary conditions at the fluid−solid interface.

The interaction between the capsule and the surface (both the undamaged region and crack wall) is modeled with a nonspecific Morse potential[1,12,13]

$$\varphi(r) = \varepsilon\left(1 - \exp\left[-\frac{(r - r_0)}{\kappa}\right]\right)^2 \quad (3)$$

where ε and κ characterize the respective strength and range of the interaction potential. Additionally, r is the distance between the LSM node and the substrate surface, and r_0 is the distance at which this force is equal to zero. In all of our simulations, we set $\kappa = 1$ and $r_0 = 1$, while ε was varied to determine the effect of the adhesion force on the microcapsule's motion.

To capture the diffusion of nanoparticles within the encapsulated fluid, we use a Brownian dynamics model for the particles.[1,17,27] The nanoparticles trajectories obey a stochastic differential equation

$$d\boldsymbol{r}(t) = \boldsymbol{u}(\boldsymbol{r},t)dt + \sqrt{2D_0}d\boldsymbol{W}(t) \quad (4)$$

where the first term describes the advection due to the local fluid velocity $\boldsymbol{u}(r,t)$ and the second term describes the particle's Brownian motion, with D_0 being the particle's diffusion coefficient and $d\boldsymbol{W}(t)$ being the differential of a Weiner process with unit variance. We neglect backflow effects (*i.e.*, the impact of the particles' motion on the flow field); the latter assumption is valid for submicrometer sized particles at relatively low concentrations. We also neglect the interactions between the particles. We use a first-order Euler scheme method to solve eq 4.[17] Note that an ensemble average of the particle trajectories computed from eq 4 is equivalent to solving the convection−diffusion equation for the concentration of nanoparticles.[17,28,29]

We simulate the chemisorption of nanoparticles onto the crack walls by assigning a probability w_{dep} for a nanoparticle to deposit from the microcapsule's interior onto the surface in a given time step Δt. (Note that the nanoparticles can only bind to the surface when the microcapsule is localized in the crack.) This probability has the form

$$w_{dep} = k\Delta t e^{-r/r_{tun}} \quad (5)$$

Here r is the distance from the microcapsule's shell to the crack wall, r_{tun} is a characteristic distance over which the probability decays, and k is a characteristic deposition rate, which was set to $k = 1/\Delta t$ in our simulations. We also set the characteristic tunneling distance r_{tun} in eq 5 equal to the distance κ in the Morse potential (in eq 3). A "rejection" rule[28,30] is applied to those nanoparticles that are not deposited onto the surface at a given time step (*i.e.*, with a probability $(1 - w_{dep})$); the variable $\Delta\boldsymbol{W}$ is set equal to zero for the "rejected" particles, and their positions are then updated in accordance with eq 4.

The profile of the substrate−fluid interface is updated dynamically at each time step; the local elevation of the profile due to the nanoparticle deposition is computed as $h = (4\pi/3)r_{np}^3 n$, where n in the density of deposited nanoparticles at the wall at a given point. The radius of the nanoparticles, r_{np}, is taken to be 10^3 times smaller than the radius of the microcapsule.

Finally, we note that we have presented just one methodology for healing materials. We refer the reader to refs 31−38 for papers describing additional approaches of achieving materials repair at the nano- and microscales.

Acknowledgment. A.C.B. gratefully acknowledges financial support from the ONR (for partial support of A.C.B.) and DOE (for partial support of G.V.K). G.V.K. acknowledges partial support from NSF through the TeraGrid resources provided by NCSA. T.P.R. acknowledges support by the U.S. Department of Energy, Office of Basic Energy Science, the Army Research laboratory through the MURI program, and the NSF supported MRSEC at the University of Massachusetts Amherst. T.E. and A.C. also acknowledge support from the MRSEC at the University of Massachusetts Amherst.

REFERENCES AND NOTES

1. Verberg, R.; Dale, A. T.; Kumar, P.; Alexeev, A.; Balazs, A. C. Healing Substrates with Mobile Particle-Filled Microcapsules: Designing a 'Repair and Go' System. *J. R. Soc. Interface* **2007**, *4*, 349–357.
2. Breitenkamp, K.; Emrick, T. Novel Polymer Capsules from Amphiphilic Graft Copolymers and Ring-Opening Cross Metathesis. *J. Am. Chem. Soc.* **2003**, *125*, 12070–12071.
3. Lin, Y.; Skaff, H.; Emrick, T.; Dinsmore, A. D.; Russell, T. P. Nanoparticles at Liquid−Liquid Interfaces: Assembly, Displacement and Transport. *Science* **2003**, *299*, 226–229.
4. Boker, A.; He, J.; Emrick, T.; Russell, T. P. Self-Assembly of Nanoparticles at Interfaces. *Soft Matter* **2007**, *3*, 1231–1248.

5. Gupta, S.; Zhang, Q. L.; Emrick, T.; Balazs, A. C.; Russell, T. P. Entropy-Driven Segregation of Nanoparticles to Cracks: A Route to Self-Healing Systems. *Nat. Mater.* **2006**, *5*, 229–233.
6. Balazs, A. C.; Emrick, T.; Russell, T. P. Nanoparticle−Polymer Composites: Where Two Small Worlds Meet. *Science* **2006**, *314*, 1107–1110.
7. Revanur, R.; McCloskey, B.; Breitenkamp, K.; Freeman, B. D.; Emrick, T. Reactive Amphiphilic Graft Copolymer Coatings Applied to Poly(vinylidene fluoride) Ultrafiltration Membranes. *Macromolecules* **2007**, *40*, 3624–3630.
8. Berdichevsky, Y.; Khandurinab, J.; Guttmanb, A.; Loa, Y.-H. UV/Ozone Modification of Poly(dimethylsiloxane) Microfluidic Channels. *Sens. Actuators, B* **2004**, *97*, 402–408.
9. Mills, K. L.; Zhu, X. Y.; Takayama, S. C.; Thouless, M. D. The Mechanical Properties of a Surface-Modified Layer on Polydimethylsiloxane. *J. Mater. Res.* **2008**, *23*, 37–48.
10. Crosby, A. Private communication.
11. Buxton, G. A.; Verberg, R.; Jasnow, D; Balazs, A. C. Newtonian Fluid Meets an Elastic Solid: Coupling Lattice Boltzmann and Lattice Spring Models. *Phys. Rev. E* **2005**, *71*, 056707-18.
12. Alexeev, A.; Verberg, R.; Balazs, A. C. Designing Compliant Substrates to Regulate the Motion of Vesicles. *Phys. Rev. Lett.* **2006**, *96*, 148103.
13. Alexeev, A; Verberg, R.; Balazs, A. C. Modeling the Motion of Microcapsules on Compliant Polymeric Surfaces. *Macromolecules* **2005**, *38*, 10244–10260.
14. Alexeev, A.; Balazs, A. C. Designing Smart Systems To Selectively Entrap and Burst Microcapsules. *Soft Matter* **2007**, *3*, 1500–1505.
15. Usta, O. B.; Alexeev, A.; Balazs, A. C. Fork in the Road: Patterned Surfaces Direct Microcapsules to Make a Decision. *Langmuir* **2007**, *23*, 10887–10890.
16. Alexeev, A.; Verberg, R.; Balazs, A. C. Patterned Surfaces Segregate Compliant Microcapsules. *Langmuir* **2007**, *23*, 983–987.
17. Verberg, R.; Alexeev, A.; Balazs, A. C. Modeling the Release of Nanoparticles from Mobile Microcapsules. *J. Chem. Phys.* **2006**, *125*, 224712.
18. Usta, O. B.; Alexeev, A.; Zhu, G.; Balazs, A. C. Modeling Microcapsules That Communicate through Nanoparticles To Undergo Self-Propelled Motion. *ACS Nano* **2008**, *2*, 471–476.
19. Therriault, D; White, S. R.; Lewis, J. A. Chaotic Mixing in Three-Dimensional Microvascular Networks Fabricated by Direct-Write Assembly. *Nat. Mater.* **2003**, *2*, 265–271.
20. Stone, H. A.; Stroock, A. D.; Ajdari, A. Engineering Flows in Small Devices: Microfluidics Toward a Lab-on-a-Chip. *Ann. Rev. Fluid Mech.* **2004**, *36*, 381–411.
21. Dubreuil, F.; Elsner, N.; Fery, A. Elastic Properties of Polyelectrolyte Capsules Studied by Atomic-Force Microscopy and RICM. *Eur. Phys. J. E* **2003**, *12*, 215–221.
22. Elsner, N.; Kozlovskaya, V.; Sukhishvili, S. A.; Fery, A. pH-Triggered Softening of Crosslinked Hydrogen-Bonded Capsules. *Soft Matter* **2006**, *2*, 966–972.
23. Succi, S. *The Lattice Boltzmann Equation for Fluid Dynamics and Beyond*; Clarendon Press: Oxford, 2001.
24. Ladd, A. J. C.; Kinney, J. H.; Breunig, T. M. Deformation and Failure in Cellular Materials. *Phys. Rev. E* **1997**, *55*, 3271–3275.
25. Buxton, G. A.; Care, C. M.; Cleaver, D. J. A Lattice Spring Model of Heterogeneous Material with Plasticity. *Modell. Simul. Mater. Sci. Eng.* **2001**, *9*, 485–497.
26. Lallemand, P.; Luo, L.-S. Theory of the Lattice Boltzmann Method: Dispersion, Dissipation, Isotropy, Galilean Invariance, and Stability. *Phys. Rev. E* **2000**, *61*, 6546–6562.
27. Verberg, R; Yeomans, J. M.; Balazs, A. C. Modeling the Flow of Fluid/Particle Mixtures in Microchannels: Encapsulating Nanoparticles within Monodisperse Droplets. *J. Chem. Phys.* **2005**, *123*, 224706.
28. Szymchak, P.; Ladd, A. J. C. Boundary Conditions for Stochastic Solutions of the Convective-Diffusion Equations. *Phys. Rev. E* **2003**, *68*, 036704.
29. Ottinger, H. C. *Stochastic Processes in Polymeric Fluids*; Springer: Berlin, 1996.
30. Cali, A.; Succi, S.; Cancelliere, A.; Benzi, R.; Gramignani, M. Diffusion and Hydrodynamic Dispersion with the Lattice Boltzmann Method. *Phys. Rev. A* **1992**, *45*, 5771–5774.
31. Caruso, M. M.; Davis, D. A.; Shen, Q.; Odom, S. A.; Sottos, N. R.; White, S. R.; Moore, J. S. Mechanically-Induced Chemical Changes in Polymeric Materials. *Chem. Rev.* **2009**, *109*, 5755–5798.
32. Chen, X.; Dam, M. A.; Ono, K.; Mal, A; Shen, H; Nutt, S. R.; Sheran, K.; Wudl, F. A Thermally Re-mendable Cross-Linked Polymeric Material. *Science* **2002**, *295*, 1698–1702.
33. Cordier, P.; Tournilhac, F.; Soulie-Ziakovic, C.; Leibler, L. Self-Healing and Thermoreversible Rubber from Supramolecular Assembly. *Nature* **2008**, *451*, 977–980.
34. Amendola, V.; Meneghetti, M. Self-Healing at the Nanoscale. *Nanoscale* **2009**, *1*, 74–88.
35. Trask, R. S.; Williams, H. R.; Bond, I. P. Self-Healing Polymer Composites: Mimicking Nature to Enhance Performance. *Bioinspiration Biomimetics* **2007**, *2*, P1–P9.
36. Balazs, A. C. Modeling Self-Healing Materials. *Mater. Today* **2007**, *10*, 18–23.
37. Wool, R. A. Self-Healing Materials: A Review. *Soft Matter* **2008**, *4*, 400–418.
38. Wu, D. Y.; Meure, S; Solomon, D. Self-Healing Polymeric Materials: A Review of Recent Developments. *Prog. Polym. Sci.* **2008**, *33*, 479–522.